ADVANCED MATERIALS INTERFACES
www.advmatinterfaces.de

Structure Formation of C_{60} on Insulating CaF_2 Substrates: Matching Experiments with Simulations

*William Janke, Lukas Höltkemeier, Angelika Kühnle, and Thomas Speck**

The epitaxial growth of metallic thin films has been studied intensively, leading to computational models that can predict diverse morphologies depending on thermodynamic and kinetic growth parameters. Much less is known about thin films of organic molecules. Here kinetic Monte Carlo simulations to study buckyball C_{60} molecules on dielectric CaF_2(111) substrates is employed. This system undergoes a transition from mostly one-layered growth to two-layered growth of triangular cluster morphologies as the temperature is raised. Even though simplified, these simulations still require a large set of parametrized rates for the elementary transitions, the determination of which has been challenging. Here recent results for these parameters to measure cluster densities and second layer occupations are employed. Simulation snapshots of cluster morphologies are compared in a wide range of temperatures to test to which extent rate models can match the experimental observations. While adjustments to free diffusion parameters are necessary to reproduce the experimentally observed cluster densities and sizes, the cluster morphologies are excellently reproduced without further adjustments.

1. Introduction

The self-assembly of organic thin films on metallic[1,2] and dielectric surfaces[3] has received considerable attention driven by the prospect of applications in fields like organic electronics[4] and photovoltaics.[5] A wide variety of complex nanostructures can be produced via epitaxy—the controlled deposition of particles on surfaces—depending on the choice of adsorbate/substrate materials and their interaction with each other, as well as experimental parameters like particle flux and substrate temperature.[6–9]

An extensively studied organic molecule that has become a paradigmatic choice as an adsorbate for deposition experiments is the fullerene C_{60}, which has been shown to produce a vast assortment of resulting cluster morphologies on metallic[10–15] and insulating[16–34] substrates. However, even for the self-assembly of such a well-studied molecule, reliable structure predictions and design principles are mostly lacking. Computer simulations can be used to fill this gap and to explore the parameter space efficiently. While first principle and atomistic simulations can account for molecular details, they are prohibitively expensive to access the length and time scales needed to determine cluster morphologies. On large lengths, continuum approaches[35] including phase-field modeling[36] require the input of effective parameters (mobilities, interfacial tensions, etc.). An intermediate particle-resolved technique is the kinetic Monte Carlo (KMC) method, which has been shown to be able to achieve the necessary length and time scales to simulate the cluster growth of several deposition experiments.[37–43] KMC stochastically advances a number of molecules moving between discrete lattice sites through elementary transitions that depend on the interactions with neighboring molecules.

A major issue one faces with KMC simulations is the modeling of the elementary transition rates of the system, which can involve a large amount of free parameters. Typically one reduces that amount by assuming an Arrhenius law for the transition rates and by applying some constraints (like bond counting approaches) on the remaining energy barrier and attempt rate parameters. Pure top-down modeling can easily lead to models that are oversimplified, contain invalid assumptions, or can lead to model parameters that lose their intended physical interpretation. Experimental data is used to tune the remaining parameters of such rate models and one can make use of machine learning techniques[44,45] to optimize the parameter tuning. However, experimental data alone is often insufficient to determine the transition rates of all relevant elementary processes (free diffusion, edge diffusion, ascension, descension, dissociation, etc.).

A bottom-up approach to help with the determination of KMC rate models is the use of molecular dynamics (MD) simulations. By assuming interaction potentials for the adsorbate and substrate interactions, one can set up systems in which one can directly measure the transition rates of interest.[37] In refs. [46,47] we have recently developed such an approach and gathered an extensive amount of data from MD simulations to inform KMC rate models

W. Janke, T. Speck
Institut für Physik
Johannes Gutenberg-Universität Mainz
Staudingerweg 7-9, 55128 Mainz, Germany
E-mail: thomas.speck@uni-mainz.de
L. Höltkemeier, A. Kühnle
Fakultät für Chemie
Universität Bielefeld
33501 Bielefeld, Germany

The ORCID identification number(s) for the author(s) of this article can be found under https://doi.org/10.1002/admi.202201510.

DOI: 10.1002/admi.202201510

for the epitaxial growth of C_{60} on $CaF_2(111)$. These papers have resulted in a parameter-free rate model for C_{60} on $C_{60}(111)$ diffusive processes (processes in the second layer and higher), as well as two distinct rate models for C_{60} on $CaF_2(111)$ diffusion with one free parameter each (for processes in the first layer). Here, we test these rate models against experimental observations.

2. Modeling

To model the epitaxial growth of C_{60} on $CaF_2(111)$ we implemented a rejection-free KMC simulation. The atomistic triangular surface lattice of the $CaF_2(111)$ substrate ($a_{CaF_2(111)} \approx 386$ pm) is coarse-grained into a hexagonal honeycomb lattice with a lattice constant of $a = 1$ nm (**Figure 1**a), enabling the use of the same lattice structure in all layers of the simulation as it replicates the surface lattice of $C_{60}(111)$.

Deposition of particles onto the substrate with area A is implemented via an effective constant particle flux F, which enters the KMC algorithm through an area-dependent transition rate $k_{Dep} = FA$ that places particles on random lattice sites with uniform probability. Desorption of particles is neglected. We assume the substrate to be perfectly clean and flat, neglecting all kinds of possible impurities of the surface (vacancies, step edges, and adsorbed residual gas particles). Transition rates for all kinds of surface diffusion processes are calculated from attempt rates $\nu_{0,i}(n)$ and energy barriers $\Delta E_i(n)$ via the Arrhenius law[48]

$$k_i(n,T) = \nu_{0,i}(n) e^{-\Delta E_i(n)/k_B T} \tag{1}$$

with Boltzmann constant k_B, substrate temperature T, transition type $i \in \{FD/Diss/ED/Asc/Desc/...\}$ (cf. Figure 1b), and number of initial lateral neighbors n. Lateral neighbors contribute a bond energy E_B to the energy barrier of a transition if their bond has to be broken during the transition of a particle. The dependence of the energy barriers $\Delta E_i(n)$ on n can therefore be described by the bond counting approach

$$\Delta E_i(n) = \Delta E_{i,0} + (n - \hat{n}_i) E_B \tag{2}$$

where $\Delta E_{i,0}$ is a base energy barrier for transitions of type i and $\hat{n}_i$ is the number of bonds that can be sustained throughout transitions of type i (e.g., $\hat{n}_{Diss} = 0$, $\hat{n}_{ED} = 1$, $\hat{n}_{Asc} = 2$). The parameters $\Delta E_{i,0}$ and $\nu_{0,i} = \nu_0$ for the second and higher layers (C_{60} on $C_{60}(111)$ diffusion), as well as the effective bond energy $E_B = 235$ meV (for all layers), are based on MD simulations of coarse-grained C_{60} molecules interacting via the Girifalco potential[49,50] and taken from the "Simple" model described in ref. [46]. For the diffusive transitions in the first layer, we have previously conducted MD simulations of C_{60} on $CaF_2(111)$ with an atomistic (rigid-body) and a coarse-grained (Girifalco-like) representation of the C_{60} molecule and have derived rate models for the transition rates of both models with a single free parameter (ε_F) which determines the interaction strength between the C_{60} molecule and the fluoride ions of the $CaF_2(111)$ surface.[47] Hence, the base energy barriers $\Delta E_{i,0}(\varepsilon_F)$ and attempt rates $\nu_{0,i}(\varepsilon_F)$ for the processes in the first layer have an additional dependence on the free model parameter ε_F. To achieve an adsorbate-substrate interaction that is somewhat weaker than the adsorbate–adsorbate interaction (such that the observed two-layered cluster morphologies can evolve), we expect the interaction parameter to fall into the range $\varepsilon_F \in [35, 55]$ meV to reproduce the experiments. In the following, we scrutinize the atomistic and coarse-grained model of ref. [47].

Our implementation also supports transitions to and from "overhang"-sites (i.e., sites that are not fully supported by three particles in the layer below denoted as "OH" in Figure 1b), for which we have not gathered MD simulation data. Based on transition state theory and the involved interaction potentials, there is no evidence that the transition pathways via overhang sites are significantly suppressed. Therefore, we include them at least approximately and assign them as follows: The overhang sites can be reached through ascension or descension with transition rates equal to the ascension and descension rates that we have measured in MD simulation with normal target sites. Once a particle is on an overhang site, the transition rates of outgoing transitions are chosen based on our transition rate measurements of C_{60} on $C_{60}(111)$ with ascension/descension transitions that are modeled as a free diffusion process (with bond-counting as in Equation (2) and $\hat{n}_{Asc/Desc,OH} = 2$) and with edge-diffusion transitions that are modeled as the A step edge diffusion transitions on a fully covered $C_{60}(111)$ surface.

3. Results

3.1. Cluster Densities

For free surface diffusion, a strong discrepancy between the parameters obtained from MD simulations (diffusion barriers

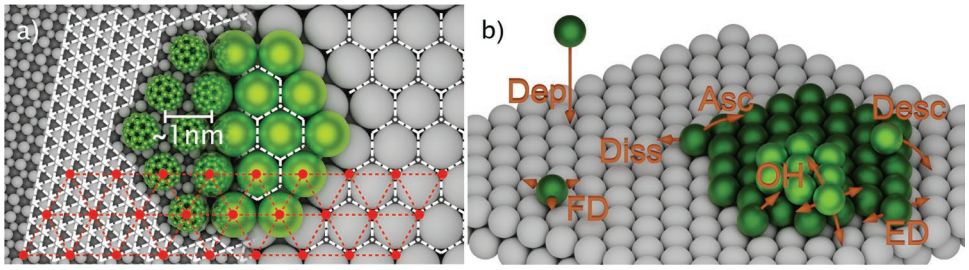

Figure 1. Details of the KMC implementation. a) Coarse-graining of the triangular $CaF_2(111)$ surface lattice (left) to a hexagonal honeycomb lattice identical to the $C_{60}(111)$ surface lattice (right). The overlayed red lattice illustrates the overlap with the triangular lattice of a compact C_{60} cluster. b) Visualization of the implemented transition types. In addition to deposition (Dep) and free diffusion (FD), various diffusion transitions of particles in a cluster are realized: dissociation (Diss), ascension (Asc), descension (Desc), edge diffusion (ED). Also implemented are transitions to and from overhang sites (OH)—sites that are not fully supported by three particles in the layer below.

ΔE_{FD} in the range 20 – 90 meV) and from experimental cluster density measurements (estimated diffusion barrier of $\Delta E_{FD,\ Exp} \approx 214(16)$ meV[22]) is observed.[47] Our first test is to check if the rate models derived from the MD simulations carry this discrepancy over into cluster densities that we can measure in KMC simulations. The experimental cluster densities were obtained in deposition experiments after a 4 min deposition phase with a particle flux of $F \approx 0.026$ ML min^{-1} (monolayers per minute).[22] Data for temperatures $T = 297$ K and $T = 319$ K is based on AFM images published in ref. [38], which were captured with the same experimental setup after a 2 min deposition phase.

On the simulation side, we run KMC simulations with a flux of $F = 0.026$ ML min^{-1} at temperatures $T \in \{96, 120, 137, 144, 160, 190, 217\}$ K with a 4 min deposition phase and at temperatures $T \in \{240, 260, 280, 297, 319\}$ K with a 2 min deposition phase, and measure the resulting cluster densities (as an ensemble average calculated from 20 runs per temperature). For this set of simulations, we use system sizes of up to $L = 2000$ corresponding to an area of $A = \Omega L^2 = 3.464$ µm^2, where $\Omega = 0.866$ nm^2 is the area of a surface lattice unit cell corresponding to the area covered by a single C_{60} molecule. We measure the cluster density per adsorption site

$$\Omega N = \frac{N_C \Omega}{A} = \frac{N_C}{L^2} \tag{3}$$

where N_C is the number of clusters that have formed in the simulation box shortly after the deposition phase. There is a smallest measurable cluster density (if only single clusters are formed in the whole simulation box) that is marked as the light gray line in **Figure 2**.

An Arrhenius plot of simulation results in comparison with the experimental data is shown in Figure 2. We see that the original diffusion rates of the atomistic and coarse-grained rate models generate much lower cluster densities (orange squares and yellow diamonds in Figure 2) than the experiment in the whole temperature range even using a high value for the adparticle-substrate interaction parameter of $\varepsilon_F = 55$ meV. This deviation was expected and, as already discussed in ref. [47], we propose that it can be explained by the presence of impurities on the experimental $CaF_2(111)$ surfaces (so-called "impurity-trapping"[51]), for example, water particles adsorbed during preparation and deposition from the imperfect vacuum, which can act as nucleation sites for the deposited C_{60} molecules.

To test if the other transitions of the rate models (besides the free diffusion rate) produce results compatible with the experiment, we adjust the free diffusion process to closely reproduce the experimental cluster densities. Testing out constant values for the diffusion barrier ΔE_{FD} and attempt rate $\nu_{0,FD}$, we are not able to find a pair of parameters that reproduces the experiment well in the full temperature range. Two examples are given in Figure 2, with one coming very close to reproducing the low to mid temperature range (light green triangles) while the other one yields better results for the high temperature range (dark green triangles). Overall, we find that the low temperature regime is better described by larger diffusion barriers, approaching values of up to $\Delta E_{FD} = 250$ meV (with attempt rates of up to 10×10^{17} Hz), while the high temperature

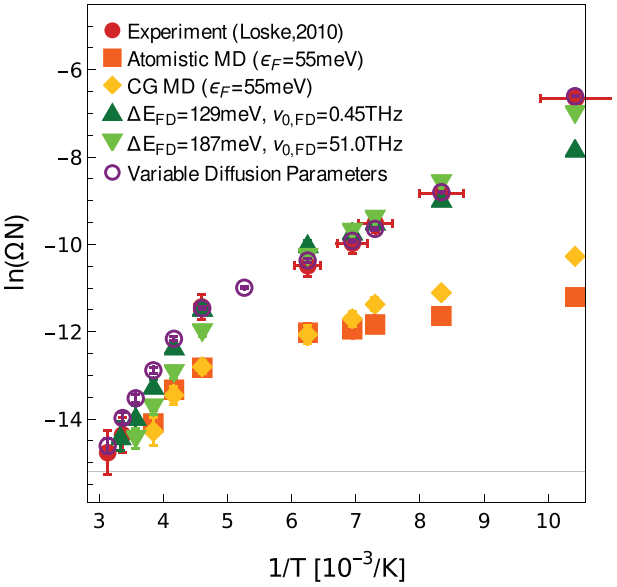

Figure 2. Arrhenius plot of the cluster densities (per adsorption site) from experimental measurements (red circles, data from refs. [22, 38]) in comparison with measurements from KMC simulations using various models for the free diffusion parameters as described in the main text. The gray horizontal line denotes the minimal obtainable cluster density on the simulated surface area of $A = \Omega L^2 = 3.464$ µm^2. Data points that come close to this boundary line are omitted from the plot. Each simulation data point is calculated from a sample size of $n_s = 20$ simulations.

regime is better reproduced using low energy barriers (as low as $\Delta E_{FD} = 100$ meV with attempt rates as low as 10×10^{11} Hz). Therefore, to capture the experimental cluster densities over the whole temperature range, we model the diffusion barrier and the order of magnitude of the attempt rates with a linear dependence on the inverse temperature,

$$\Delta E_{FD}\left(\frac{1}{T}\right) = 0.061\ eV + 19.61\ \text{eV K} \times \frac{1}{T} \tag{4}$$

$$\nu_{0,FD}\left(\frac{1}{T}\right) = \exp\left(19.26 + 1981\ \text{K} \times \frac{1}{T}\right) Hz \tag{5}$$

Figure 2 shows that these variable diffusion parameters (open purple circles) fit the experimental data very well. Such a temperature dependence of the effective free diffusion parameters agrees with our proposition of adsorbed impurities on the experimental surface, as such an effect will also vary with the substrate temperature. One can expect that lower temperatures lead to a higher tendency to adsorb impurities, leading to the observed steeper increase of cluster densities toward lower temperatures.

An interesting observation of the experimental cluster densities is the large slope of the Arrhenius data at high temperatures above $T \approx 200$ K (cf. Figure 2). While one might suspect that this is caused by a crossover in diffusive behavior (as it was observed in the MD simulations of refs. [47, 52]), this feature is present in our simulation results independent of the used free diffusion model and is therefore not generated by a sudden increase of the free diffusion rate. Rather, it can be explained as a result of

hindered nucleation due to the decreasing stability of small clusters at higher temperatures. In nucleation theory,[51] the effect of cluster stability on the cluster density (per adsorption site),

$$\Omega N \approx \eta \left(\frac{\Omega^2 F}{D} \right)^{\frac{i^*}{i^*+2}} e^{E_{i^*}/(i^*+2)k_B T} \tag{6}$$

is taken into account via the critical cluster size i^* and the critical cluster energy E_{i^*}. Here, the diffusion coefficient

$$D = \frac{1}{4} l^2 \nu_{0,\mathrm{FD}} e^{-\Delta E_{\mathrm{FD}}/k_B T} \tag{7}$$

is determined by the free diffusion parameters (ΔE_{FD} and $\nu_{0,\mathrm{FD}}$) and the jump length l. The predictions of Equations (6) and (7) match the results of our KMC simulations in the low temperature regime very well for parameters $\eta \simeq 0.13$, $i^* \simeq 1.0$ and $E_{i^*} \simeq 0$ meV (green dashed line in **Figure 3**a). This set of parameters is in line with the expectation that monomers are critical clusters ($i^* = 1$) at low temperatures, where dimers can already be considered as stable. When looking at temperatures above 200 K, the experimental and simulated densities start to strongly deviate from this prediction, hinting at an increase of the critical cluster size. To capture this behavior we introduce a simple linear dependence of the parameters i^* and E_{i^*} (plotted in Figures 3b,c) via

$$i^*(T) = \begin{cases} 1 & T < T_1 \\ 1 + \dfrac{(T - T_1)}{(T_2 - T_1)} & T \geq T_1 \end{cases} \tag{8}$$

$$E_{i^*}(T) = [i^*(T) - 1] E_B \tag{9}$$

with temperatures $T_1 \simeq 205$ K (where the deviation from $i^* \approx 1.0$ starts), $T_2 \simeq 285$ K (where $i^* \approx 2.0$), and the bond energy $E_B = 235$ meV (chosen as discussed in Section 2). The model prediction of Equations (6) and (7) in combination with the parameters of Equations (8) and (9) is plotted as the solid line in Figure 3a, now showing excellent agreement with the simulation results.

In passing, we note that combining Equations (4),(5), and (7) into the diffusive time $\tau = l^2/4D$ leads to a super-Arrhenius behavior

$$\ln(\tau / \tau_0) = J^2 \left(\frac{1}{T} - \frac{1}{T_0} \right)^2 \text{ for } T < T_0 \tag{10}$$

also found for the structural relaxation time of glass-forming liquids.[53,54] The parameters of Equation (10) for our effective free diffusion model are $J \approx 477$ K, $T_0 \approx 357.5$ K, and $\log(\tau_0) \approx -21.04$.

3.2. Second Layer Occupation

The deposition experiments in ref. [38] have shown that C_{60} epitaxy on CaF_2(111) undergoes a transition from mostly one-layered growth to two-layered growth of triangular cluster morphologies at $T = 319$ K with interesting complex morphologies in the transition regime. Since the coverage of the second layer during growth is mainly governed by the ascension rate, which is strongly affected by our model parameter ε_F, we use this observation to tune the value of the remaining free parameter ε_F. We again employ a molecular flux of $F = 5 \times 10^{-4}$ s^{-1} nm^{-2} $\approx$ 0.026 ML min^{-1} applied during a two minute deposition phase employing periodic simulation boxes with area $A = 3.464$ μ m^2 ($L = 2000$) and substrate temperatures $T \in [270, 325]$ K. Simulations are run for both the atomistic and coarse-grained rate model and the model parameter ε_F is varied in the range $\varepsilon_F \in [40, 50]$ meV. We measure the second layer occupation $\Lambda_2 = N_2/N_1$ immediately after the deposition phase, where N_i denotes the number of particles in the ith layer. To reproduce

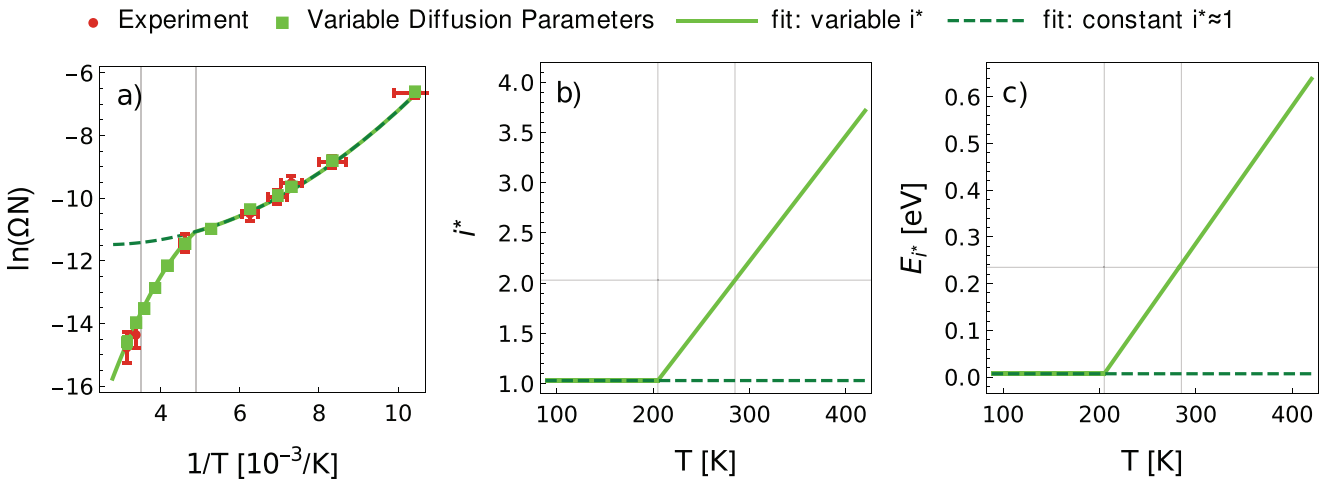

Figure 3. a) Cluster densities (per adsorption site) comparing experiment (red symbols) with KMC simulations (green symbols, using Equations (4) and (5)) and nucleation theory (solid and dashed line from Equation (6) with fixed prefactor $\eta \approx 0.13$). b) Model parameters i^* and c) E_{i^*} as function of temperature T. The green dashed line uses a constant value of $i^* \approx 1$ and the light green line uses a linear increase of i^* above a temperature $T_1 \approx$ 205 K (cf. Equation (8)).

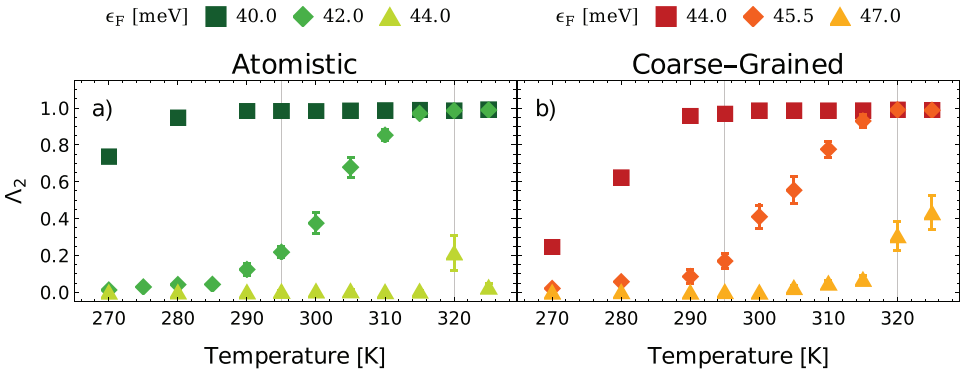

Figure 4. Second layer occupation Λ_2 after the deposition phase plotted against temperature for a) the atomistic and b) coarse-grained rate model. The shown ε_F values (within ≈5% of the optimal values) shows nicely how strongly the transition temperature is affected by the choice of ε_F. Data points are calculated from sample sizes of $n_s = 4$ simulations except for the optimal ε_F parameters in the transition regime, which have been sampled from $n_s = 11$ simulations.

the experiments, we seek values of ε_F at which simultaneously full coverage of the second layer ($\Lambda_2 \approx 1$) for temperatures $T \geq 320$ K and a low coverage $\Lambda_2 \approx 0.2$ at $T = 295$ K is reached. The resulting second layer occupations are plotted as a function of temperature in **Figure 4** for three ε_F values. We observe a high sensitivity of Λ_2 to the parameter ε_F in both models. In the atomistic model, the experimental observations are best reproduced at $\varepsilon_F = 42.0(5)$ meV and in the coarse-grained model at $\varepsilon_F = 45.5(5)$ meV.

With these parameters, we calculate the base ascension barriers and attempt rates (following ref. [47]). The corresponding ascension barriers, attempt rates, and resulting ascension rates (for $T = 295$ K and $T = 320$ K) are listed in **Table 1**. We conclude that the ε_F values of both our models lead to practically the same energy barriers and attempt rates (at $n = 2$) of approximately $\Delta E_{Asc}(n = 2) \approx 500$ meV and $\nu_{0,\,Asc}(n = 2) \approx 1.5$ THz. Comparing to the model of ref. [38], we find that their (assumed) attempt rate of $\nu_{12} = 1.00$ THz is quiet close to our results. However, in combination with a significantly lower energy barrier of $\Delta E_{12} = 420$ meV, their model results in much higher ascension rates at the temperatures of interest. This discrepancy might be rooted in the modeling of the free diffusion process. While we tuned the free diffusion model to reproduce the experimental cluster densities (Section 3.1), in ref. [38] the free diffusion was modeled using the parameter estimates of ref. [22], which lead to unreasonably high cluster densities in the KMC simulation in comparison to the experiment (roughly, we estimate from the provided images that the cluster densities are off by one order of magnitude). Consequently, the resulting smaller cluster sizes were compensated through higher ascension rates.

Table 1. Optimal values of ε_F for the atomistic and CG rate model and corresponding energy barriers, attempt rates, and the resulting ascension rates for the case of two initial neighbors ($n = 2$) at the temperatures of interest. The parameters used by Körner et al.[38] in KMC simulations investigating the same system are also listed for comparison.

Model	Atomistic	CG	Ref. [38]
ε_F [meV]	42.0(5)	45.5(5)	–
$\Delta E_{Asc,\,0}$ [meV]	499(10)	502(9)	$\Delta E_{12} = 420$
$\nu_{0,\,Asc}$ [THz]	1.61(7)	1.43(5)	$\nu_{12} = 1.00$
k_{Asc}(295 K) [kHz]	4.81	3.79	66.79
k_{Asc}(320 K) [kHz]	22.28	17.75	242.82

3.3. Cluster Morphologies

With the free diffusion process adjusted and the free parameters fixed, the two models are now ready to be tested against the experimentally observed cluster morphologies. For the simulation snapshots, we again reproduce the experimental protocol with a molecular flux of $F \approx 0.026$ ML min^{-1} applied over a deposition phase of 4 min at the lower temperatures $T \in \{120, 133, 160, 217\}$ K and 2 min at temperatures $T \in \{297, 320\}$ K. For the lower temperatures, the system size was kept the same as in the previous sections ($A = 3.464$ μm^2), while for the temperature $T \geq 217$ K we increased the size to $L = 3000$ ($A = \Omega L^2 = 7.79$ μm^2) to accommodate the growth of multiple clusters in every simulation run.

In **Figure 5**a, we present a side-by-side comparison of AFM images (the experimental images were processed to homogenize contrast and colors and to remove background noise from the substrate) and simulation snapshots. Looking at the coarse-grained model first, we find that its predicted morphologies divert from the experiments in the full temperature range, producing exaggerated triangular star shapes at low temperatures and triangular (instead of hexagonal) base clusters at the higher temperatures. This mismatch can be explained by the large difference between A and B step edge diffusion that was measured in the coarse-grained MD simulations. In contrast, the rate model derived from the atomistic MD simulations (which only showed a slight difference between A and B step edge diffusion), produces results that are remarkably close to the experimental observations at all temperatures, transitioning from slightly star shaped clusters at low temperatures to hexagonal one-layered clusters in the mid-temperature range and finally to the growth of triangular two-layered clusters at high temperatures. Also, we observe more complex morphologies in the transition regime (at $T =$ 297 K) with partially covered second layers that grow on top

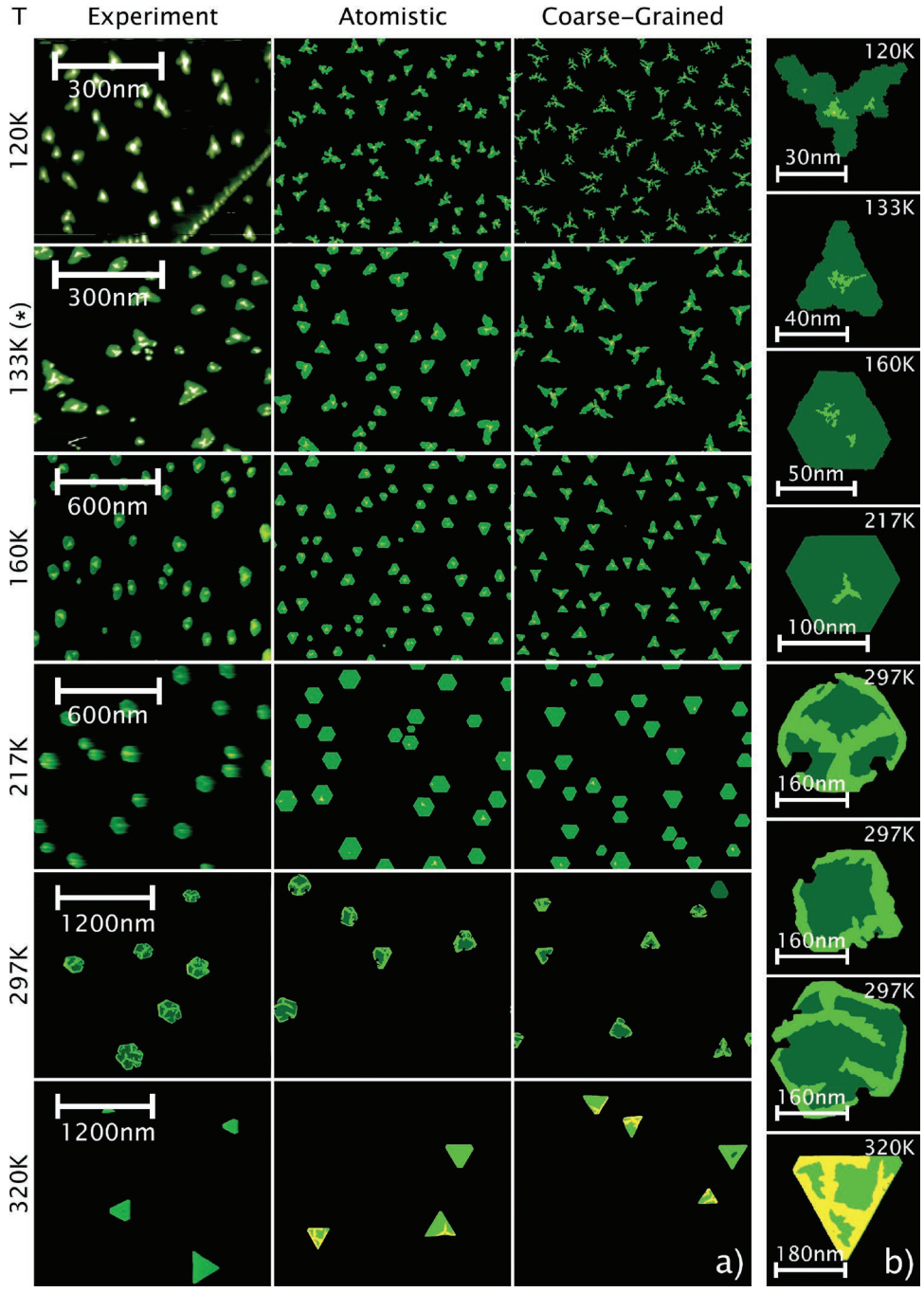

Figure 5. a) Comparison of cluster morphologies observed in experiment (left) to KMC simulation results employing the atomistic (center) and coarse-grained (right) rate model. Molecules in the first layer appear as dark green and in the second layer bright green. The experimental images have been enhanced (adjusted contrast, color range, and removed noise from the substrate surface). The measurement at $T = 133$ K was obtained using the Omicron VT-AFM-XA with the temperature estimated by matching the cluster density (Figure 3a). All other experimental measurements were obtained with the RHK 750. b) Close-ups of example clusters obtained from KMC simulations using the atomistic model for various temperatures. For $T = 297$ K multiple clusters are shown and one can see how the position of the second layer nuclei determines the exact shape of the final cluster morphology. At $T = 320$ K the simulations of both models produce a fraction of clusters with an occupation of the third layer (yellow), which is not observed in experiments.

of hexagonal base clusters into branched structures and outer layer rims.

Close-up snapshots of selected clusters are shown in Figure 5b to present a clearer view on the cluster morphologies. Now some minor differences can be spotted between the results of the atomistic model and the experiments. While in the experiments the morphologies at room temperature $T = 297$ K seem to mostly maintain the hexagonal shape of the

base cluster, the clusters in the simulation turn into more random rounded shapes. Moreover, both rate models lead to a premature formation of third-layer nuclei at $T = 320$ K, which was not observed at these low coverages in the experiments. Both of these differences might be due to our ad hoc modeling of the transition rates that involve overhang sites (Section 2), which is not based on direct measurements of those transitions in MD simulations. It is possible that these rates overestimate the frequency of transition paths from the first to the third layer and underestimate the frequency of transition paths from the first to the second layer when other molecules at clusters edge are involved.

To elucidate the complex morphologies at room temperature with populated second-layer rims (cf. Figure 5b), a previous study[38] put forward the idea of facilitated dewetting, in which molecules in the second layer facilitate ascension. This mechanism was implemented into the rate model by using a different bond counting approach that not only considered the initial number of neighbors for the determination of energy barriers (as in Equation (2)), but also the final number of neighbors. This leads to significantly reduced ascension barriers if the target sites have lateral neighbors, simulating a kind of "pulling" force exerted by particles of the second layer onto the first layer particles. However, the strength of this effect, as it was implemented in ref. [38], is at odds with our understanding of the relatively short C_{60}–C_{60} interaction range.[55] In contrast, here we have pursued a systematic route based on MD simulations without accounting for particular effects such as facilitated dewetting (at the cost of a more complex model and a more involved model parameter derivation process). Still, we obtain cluster morphologies that are in excellent agreement with the experiments.

4. Conclusion

In this paper, we have compared two rate models for KMC simulations of the epitaxial growth of C_{60} on CaF_2(111) with experimental morphologies. Both models are based on MD simulations of elementary transitions[46,47] and differ in their representation of the C_{60} molecules: either atomistic through sixty atoms in a rigid geometry, or represented as an effective bead interacting through the Girifalco potential.[49,50] The previously observed discrepancy between the free diffusion barriers of the two models with the estimated diffusion barrier from experiment[22] was carried over into the KMC simulation results with cluster densities that are much lower than in experiment. As we had measured the free diffusion rates on a clean CaF_2(111) substrate in the MD simulations—which is not something you can expect in an experiment even in ultra-high vacuum conditions—we had to adjust the free diffusion parameters to reproduce the experimental cluster densities. The diffusion barriers of the effective model range from ≈260 meV at the lower end of the temperature range to ≈120 meV at the highest temperatures, and we propose that this observed "super-Arrhenius" behavior is caused by impurities (e.g., water molecules) that have been adsorbed during preparation of the substrate and acted as traps for the deposited C_{60} molecules.

We have then tuned the remaining free model parameter ε_F for both models by looking at the second-layer occupation in the temperature range where the experiments showed a transition from one-layered to two-layered growth. We have found them to fit the experimental observation (of fully two-layered growth at $T \geq 320$ K) at a value of $\varepsilon_F = 42.0(5)$ meV for the atomistic and a value of $\varepsilon_F = 45.5(5)$ meV for the coarse-grained rate model. With those parameters, both models have ascension barriers of around $\Delta E_{Asc,\,0} \approx 500$ meV, which is in line with the expectation of an interaction between the C_{60} molecules with the CaF_2(111) surface that is somewhat weaker than the interaction of C_{60} molecules with each other (we have previously measured an ascension barrier of around 900 meV for C_{60}on C_{60}(111)[46]), which causes the evolution of interesting two-layered morphologies that have been observed close to room temperature. We have then performed simulations in the full temperature range of the experiments[22,38] to compare cluster morphologies and the transitions between different growth modes to the experimental observations. The atomistic model shows a remarkable agreement with the experiments in the full temperature range without further adjustments while the coarse-grained model fell short in reproducing the experimental morphologies. An interesting future test for the accuracy of our simulation models will be the exploration of previously unobserved cluster morphologies via time-dependent protocols, for example, through varying particle flux or substrate temperature.

5. Experimental Section

Experiments using an atomic force microscope (AFM) were performed in two different ultra-high vacuum (UHV) systems: an RHK 750 variable temperature AFM (RHK Technology, Troy, Michigan, USA) and an Omicron VT-AFM-XA (Scienta Omicron GmbH, Taunusstein, Germany). Both systems are capable of recording AFM images in frequency modulation mode at variable sample temperatures. All sample preparation and AFM imaging were performed under UHV conditions with a base pressure typically better than 10^{-10} mbar. Fluorite (CaF_2) single crystals (Korth Kristalle, Altenholz, Germany) were cleaved in situ by cutting with a scalpel at room temperature to obtain a freshly cleaved (111) surface. The cleaved crystals were degassed at temperatures between 400 and 435 K for 1.5 h prior to and after cutting.

Molecule deposition was performed by sublimation of C_{60} (purity of 99.95%, MER Corporation, Tuscon, Arizona; and 98%, Sigma Aldrich GmbH, Taufkirchen, Germany) from a home-built Knudsen cell. The parameters required for a given flux F were determined after each re-fill of the cell. To obtain a flux of $F \approx 0.026$ ML min^{-1} (monolayers per minute), the cell crucible was held at a temperature of about 560 K. During molecule deposition, the sample was stored in a manipulator that allows for cooling the sample with liquid nitrogen. Adjusting the nitrogen flow allowed for controlling the temperature of the cooling stage. The temperature was measured with a type K thermocouple positioned at the sample holder base. Thus, a temperature difference with respect to the sample surface was expected. For the RHK 750 the temperature was calibrated by a type K thermocouple glued directly onto the crystal surface, with an error estimated to be ±5 K.[22] For all other measurements, the temperature was determined indirectly through measuring island densities.

After molecule deposition, the sample was transferred into the AFM using a pre-cooled wobble stick. During the transfer, however, the sample was not cooled. Even though the transfer time was kept to a minimum, a slight rise in the temperature during transfer could not be excluded. In the AFM, the temperature was quenched to $T \leq 120$ K

by cooling with a liquid nitrogen (helium) flow cryostat and counter-heating using a pyrolytic boron nitride heater and a Lakeshore 331 temperature controller.

Statistical Analysis: The measurements of cluster densities in the simulation snapshots were obtained by counting the clusters in the simulation box with the MorphologicalComponents/ComponentMeasurements methods of Mathematica. The presented cluster densities were calculated as the mean values of sets of measurements and the corresponding error bars were the standard errors ($\sigma / \sqrt{n_s}$). The sample size for each cluster density data point was $n_s = 20$ simulations. The presented second layer occupations (Λ_2) were calculated in a similar fashion (mean/standard error) with sample sizes of $n_s = 4 - 11$ simulations depending on the data point.

Acknowledgements

The authors thank Ralf Bechstein and Felix Loske for stimulating discussions. Michael Reichling was gratefully acknowledged for access to the RHK system and valuable practical support during the measurements. The authors acknowledge funding from the Deutsche Forschungsgemeinschaft (Grant No. 319880407). All numerical computations were performed on the MOGON II cluster at ZDV Mainz.

Open access funding enabled and organized by Projekt DEAL.

Conflict of Interest

The authors declare no conflict of interest.

Data Availability Statement

The data that support the findings of this study are available from the corresponding author upon reasonable request.

Keywords

epitaxy, kinetic Monte Carlo simulations, molecular dewetting, molecular dynamics

Received: July 8, 2022
Revised: August 26, 2022
Published online: October 10, 2022

[1] J. V. Barth, *Annu. Rev. Phys. Chem.* **2007**, *58*, 375.
[2] A. Kühnle, *Curr. Opin. Colloid Interface Sci.* **2009**, *14*, 157.
[3] R. Hoffmann-Vogel, *Rep. Prog. Phys.* **2017**, *81*, 016501.
[4] D. Vuillaume, *Molecular Electronics Based on Self-Assembled Monolayers*, Oxford University Press, Oxford **2017**.
[5] M. Graetzel, R. A. J. Janssen, D. B. Mitzi, E. H. Sargent, *Nature* **2012**, *488*, 304.
[6] R. Otero, J. M. Gallego, A. L. V. de Parga, N. Martín, R. Miranda, *Adv. Mater.* **2011**, *23*, 5148.
[7] F. Kling, R. Bechstein, P. Rahe, A. Kühnle, in *Noncontact Atomic Force Microscopy* (Eds: S. Morita, F. J. Giessibl, E. Meyer, R. Wiesendanger), Vol. *3*, Springer International Publishing, Cham **2015**, pp. 147–171.
[8] M. Einax, W. Dieterich, P. Maass, *Rev. Mod. Phys.* **2013**, *85*, 921.
[9] P. Rahe, M. Kittelmann, J. L. Neff, M. Nimmrich, M. Reichling, P. Maass, A. Kühnle, *Adv. Mater.* **2013**, *25*, 3948.
[10] J. Weckesser, J. V. Barth, K. Kern, *Phys. Rev. B* **2001**, *64*, 161403.
[11] S. Guo, D. P. Fogarty, P. M. Nagel, S. A. Kandel, *J. Phys. Chem. B* **2004**, *108*, 14074.
[12] F. Loske, R. Bechstein, J. Schütte, F. Ostendorf, M. Reichling, A. Kühnle, *Nanotechnology* **2009**, *20*, 065606.
[13] R. Pawlak, S. Kawai, S. Fremy, T. Glatzel, E. Meyer, *ACS Nano* **2011**, *5*, 6349.
[14] R. Pawlak, S. Kawai, S. Fremy, T. Glatzel, E. Meyer, *J. Phys. Condens. Matter* **2012**, *24*, 084005.
[15] A. Picone, D. Giannotti, M. Riva, A. Calloni, G. Bussetti, G. Berti, L. Duò, F. Ciccacci, M. Finazzi, A. Brambilla, *ACS Appl. Mater. Interfaces* **2016**, *8*, 26418.
[16] D. Chen, D. Sarid, *Surf. Sci.* **1994**, *318*, 74.
[17] W. Chen, H. L. Zhang, H. Xu, E. S. Tok, K. P. Loh, A. T. S. Wee, *J. Phys. Chem. B* **2006**, *110*, 21873.
[18] S. Szuba, R. Czajka, A. Kasuya, A. Wawro, H. Rafii-Tabar, *Appl. Surf. Sci.* **1999**, *144–145*, 648.
[19] H. Liu, P. Reinke, *J. Chem. Phys.* **2006**, *124*, 164707.
[20] H. Shin, S. E. O'Donnell, P. Reinke, N. Ferralis, A. K. Schmid, H. I. Li, A. D. Novaco, L. W. Bruch, R. D. Diehl, *Phys. Rev. B* **2010**, *82*, 235427.
[21] S. A. Burke, J. M. Mativetsky, S. Fostner, P. Grütter, *Phys. Rev. B* **2007**, *76*, 035419.
[22] F. Loske, J. Lübbe, J. Schütte, M. Reichling, A. Kühnle, *Phys. Rev. B* **2010**, *82*, 155428.
[23] M. Groce, B. Conrad, W. Cullen, A. Pimpinelli, E. Williams, T. Einstein, *Surf. Sci.* **2012**, *606*, 53.
[24] P. Rahe, R. Lindner, M. Kittelmann, M. Nimmrich, A. Kühnle, *Phys. Chem. Chem. Phys.* **2012**, *14*, 6544.
[25] N. V. Sibirev, V. G. Dubrovskii, A. V. Matetskiy, L. V. Bondarenko, D. V. Gruznev, A. V. Zotov, A. A. Saranin, *Appl. Surf. Sci.* **2014**, *307*, 46.
[26] K. Sato, T. Tanaka, K. Akaike, K. Kanai, *Surf. Sci.* **2017**, *664*, 222.
[27] H. Mitsuta, T. Miyadera, N. Ohashi, Y. Zhou, T. Taima, T. Koganezawa, Y. Yoshida, M. Tamura, *Cryst. Growth Des.* **2017**, *17*, 4622.
[28] E. Seydel, R. Hoffmann-Vogel, M. Marz, *Nanotechnology* **2018**, *30*, 025703.
[29] A. Huttner, T. Breuer, G. Witte, *ACS Appl. Mater. Interfaces* **2019**, *11*, 35177.
[30] N. N. Nguyen, H. C. Lee, M. S. Yoo, E. Lee, H. Lee, S. B. Lee, K. Cho, *Adv. Sci.* **2020**, *7*, 1902315.
[31] L. Guo, Y. Wang, D. Kaya, R. E. Palmer, G. Chen, Q. Guo, *Nano Lett.* **2018**, *18*, 5257.
[32] K. Tanigaki, S. Kuroshima, J.-i. Fujita, T. W. Ebbesen, *Appl. Phys. Lett.* **1993**, *63*, 2351.
[33] F. Rossel, M. Pivetta, F. Patthey, E. Ćavar, A. P. Seitsonen, W.-D. Schneider, *Phys. Rev. B* **2011**, *84*, 075426.
[34] A. Matetskiy, L. Bondarenko, D. Gruznev, A. Zotov, A. Saranin, J. Chou, C. Hsing, C. Wei, Y. Wang, *Surf. Sci.* **2013**, *616*, 44.
[35] R. E. Caflisch, E. Weinan, M. F. Gyure, B. Merriman, C. Ratsch, *Phys. Rev. E* **1999**, *59*, 6879.
[36] E. Meca, J. Lowengrub, H. Kim, C. Mattevi, V. B. Shenoy, *Nano Lett.* **2013**, *13*, 5692.
[37] H. Liu, Z. Lin, L. V. Zhigilei, P. Reinke, *J. Phys. Chem. C* **2008**, *112*, 4687.
[38] M. Körner, F. Loske, M. Einax, A. Kühnle, M. Reichling, P. Maass, *Phys. Rev. Lett.* **2011**, *107*, 016101.
[39] R. A. Cantrell, P. Clancy, *J. Chem. Theory Comput.* **2012**, *8*, 1048.
[40] S. Bommel, N. Kleppmann, C. Weber, H. Spranger, P. Schäfer, J. Novak, S. Roth, F. Schreiber, S. Klapp, S. Kowarik, *Nat. Commun.* **2014**, *5*, 5388.
[41] N. Kleppmann, S. H. L. Klapp, *Phys. Rev. B* **2015**, *91*, 045436.
[42] N. Kleppmann, F. Schreiber, S. H. L. Klapp, *Phys. Rev. E* **2017**, *95*, 020801.
[43] Y. M. Acevedo, R. A. Cantrell, P. G. Berard, D. L. Koch, P. Clancy, *Langmuir* **2016**, *32*, 3045.
[44] N. Ferrando, M. A. Gosalvez, A. Ayuela, *J. Phys. Chem. C* **2014**, *118*, 11636.

[45] T. Martynec, C. Karapanagiotis, S. H. L. Klapp, S. Kowarik, *Commun. Mater.* **2021**, *2*, 90.
[46] W. Janke, T. Speck, *Phys. Rev. B* **2020**, *101*, 125427.
[47] W. Janke, T. Speck, *J. Chem. Phys.* **2021**, *154*, 234701.
[48] S. Arrhenius, *J. Phys. Chem.* **1889**, *4*, 226.
[49] L. A. Girifalco, *J. Phys. Chem.* **1991**, *95*, 5370.
[50] L. A. Girifalco, *J. Phys. Chem.* **1992**, *96*, 858.
[51] T. Michely, J. Krug, in *Islands, Mounds and Atoms*, Springer, Berlin **2004**, pp. 13–59.
[52] M. Jafary-Zadeh, C. Reddy, V. Sorkin, Y.-W. Zhang, *Nanoscale Res. Lett.* **2012**, *7*, 148.
[53] Y. S. Elmatad, D. Chandler, J. P. Garrahan, *J. Phys. Chem. B* **2009**, *113*, 5563.
[54] Y. S. Elmatad, D. Chandler, J. P. Garrahan, *J. Phys. Chem. B* **2010**, *114*, 17113.
[55] C. Chiutu, A. M. Sweetman, A. J. Lakin, A. Stannard, S. Jarvis, L. Kantorovich, J. L. Dunn, P. Moriarty, *Phys. Rev. Lett.* **2012**, *108*, 268302.